

# Recurrence required to capture the dynamic computations of the human ventral visual stream

Tim C Kietzmann<sup>1,\*</sup>, Courtney J Spoerer<sup>1</sup>, Lynn Sörensen<sup>2</sup>,  
Radoslaw M Cichy<sup>3</sup>, Olaf Hauk<sup>1</sup>,  
Nikolaus Kriegeskorte<sup>4</sup>

<sup>1</sup>MRC Cognition and Brain Sciences Unit, University of Cambridge

<sup>2</sup>Psychology Department, University of Amsterdam

<sup>3</sup>Department of Education and Psychology, Freie Universität Berlin

<sup>4</sup>Department of Psychology, Columbia University

\* Correspondence to: [tim.kietzmann@mrc-cbu.cam.ac.uk](mailto:tim.kietzmann@mrc-cbu.cam.ac.uk)

**Abstract.** The visual system is an intricate network of brain regions that enables us to recognize the world around us. Despite its abundant lateral and feedback connections, human object processing is commonly viewed and studied as a feedforward process. Here, we measure and model the rapid representational dynamics across multiple stages of the human ventral stream using time-resolved brain imaging and deep learning. We observe substantial representational transformations during the first 300 ms of processing within and across ventral-stream regions. Categorical divisions emerge in sequence, cascading forward and in reverse across regions, and Granger causality analysis suggests bidirectional information flow between regions. Finally, recurrent deep neural network models clearly outperform feedforward models in terms of their ability to jointly capture the multi-region cortical dynamics. These results establish that recurrent models are required to understand information processing in the human ventral stream.

Rapid visual recognition relies on an intricate network of interconnected cortical regions along the ventral visual pathway<sup>1</sup>. Although considerable progress has been made in characterizing the neural selectivity across much of the system, we still do not understand the underlying computations. In human neuroscience and corresponding modelling work, insight has often been generated based on time-averaged data and feedforward computational models. However, the primate visual system contains abundant lateral and feedback connections<sup>2</sup>. These give rise to recurrent interactions, which are thought to contribute to visual inference<sup>3–13</sup>. Understanding the computational mechanisms of human vision therefore requires us to measure and model the rapid representational dynamics across the different regions of the ventral stream. To accomplish this, we here combine magnetoencephalography (MEG), source-based representational dynamics analysis (RDA)<sup>14,15</sup>, and deep learning. We gain insights into the underlying computations by estimating the emergence of representational distinctions across time and ventral-stream stages and model the data using feedforward and recurrent deep neural network architectures.

Our analyses span three stages of the ventral visual hierarchy, including early- (V1-3), intermediate- (V4t/LO), and high-level (IT/PHC) visual areas<sup>16</sup>. MEG data were recorded from 15 human participants (306 sensors, two sessions each), while they viewed 92 stimuli from a diverse set of natural object categories (human and non-human faces and bodies, natural and manmade inanimate objects)<sup>17</sup>. Cortical sources were based on individual-participant reconstructions of the cortical sheet (based on anatomical MRI) and the source signals were computed using the minimum-norm estimation (MNE)<sup>18</sup>. The resulting data were subjected to a representational dynamics analysis, which reveals the rapid representational changes separately in each region of interest (ROIs). For each region and time point, RDA characterizes the underlying representation by a representational

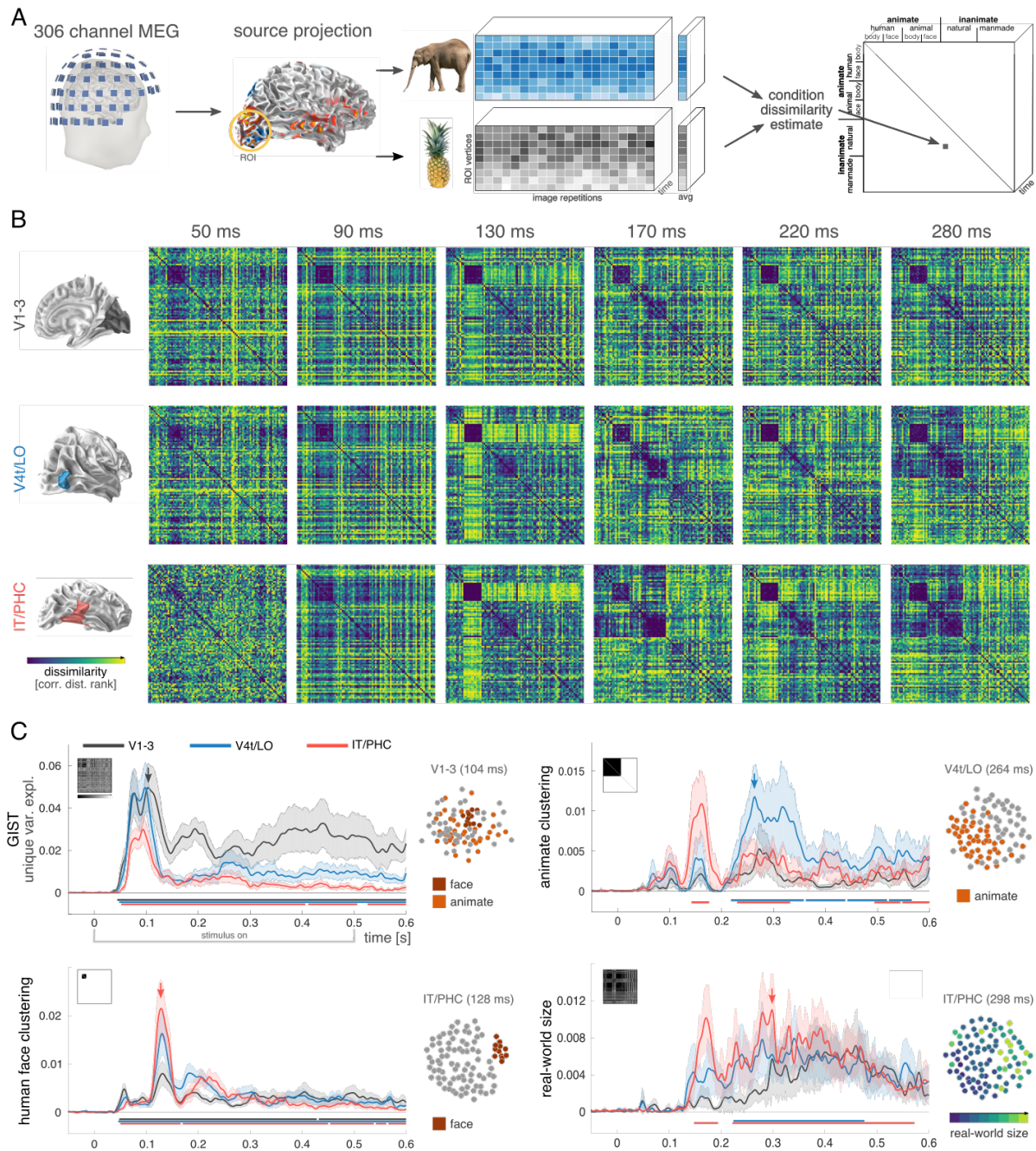
dissimilarity matrix (RDM), which indicates the degree to which different stimuli evoke similar or distinct response patterns in the neural population. For each region, the resulting RDM movie captures the dynamics as a trajectory in a high-dimensional space (Figure 1A).

Figure 1B shows participant-averaged RDMs from the three ROIs at example time points during the first 300 ms of stimulus processing (see Supplementary Movie 1 for the whole sequence). RDMs for different regions exhibit distinct representational geometries at identical time points, reflecting the fact that different regions along the ventral stream encode visual input based on different features. Conversely, RDMs for different time points for a given region exhibit substantial transformations during the first 300 ms of processing, illustrating the highly dynamic nature of the computations within each region.

To gain insight into the representational distinctions, we modelled each RDM as a nonnegative linear combination of a set of component RDMs, capturing multiple representational dimensions thought to be prominent in the ventral stream<sup>1</sup>. The linear model captures low-level features based on Gabor-wavelets (GIST<sup>19</sup>), as well as more abstract distinctions such as animacy<sup>20–22</sup>, real-world size<sup>21,23</sup>, and the category of human faces<sup>24</sup>. Finally, finer categorical distinctions were modelled following the categorical structure of the stimulus set<sup>25</sup> (see Supplementary Materials for details). The unique contribution of each model component was quantified as the extra variance explained when the component was added to the model.

Figure 1C shows how feature selectivity evolves over time in each of the ventral-stream ROIs. As expected, the unique contribution of low-level image features (GIST) emerges early in V1-3 (significant from  $\approx 40$  ms after stimulus onset, peaking at  $\approx 100$  ms) and

remains substantial and significant throughout the duration of the stimulus. GIST also contributes to explaining the early component of the IT/PHC representation, with the onset trailing V1-3 and the peak at a similar latency ( $\approx 100$  ms). However, in contrast to V1-3, the impact of the GIST component is diminished in IT/PHC (while remaining significant) as categorical components come to dominate the representational geometry in a staggered sequence. A unique contribution of the face category component emerges in IT/PHC as GIST fades (peaking at  $\approx 130$  ms in all areas). The rapid onset and strength of the face effect across ROIs are consistent with a special status of faces in the ventral stream<sup>24,26</sup>. In contrast, the superordinate division of animacy emerges in reverse cascade: It first appears as a prominent peak in IT/PHC (onset:  $\approx 140$  ms, peak:  $\approx 160$  ms), vanishes completely (returning to non-significance at  $\approx 200$  ms), and then appears as a prominent peak in V4t/LO (onset:  $\approx 220$  ms, peak:  $\approx 260$  ms), simultaneously resurfacing in IT/PHC, albeit less strongly. These results appear difficult to reconcile with a feedforward model. The staggered emergence of representational distinctions (low-level features, faces, animacy) in a given region, the temporary waning of previously prominent divisions (GIST, faces, animacy), and the reverse cascaded emergence of animacy, all occurring while the stimulus is still on (500 ms), suggest highly dynamic recurrent computations.



**Figure 1. Representational dynamics analysis (RDA) reveals how feature selectivity emerges over time along distinct ventral stream regions.** (A) RDA pipeline to extract source-space RDM movies. (B) Participant-averaged RDMs (ranked) for regions V1-3, V4t/LO, and IT/PHC at selected time-points. All ROIs exhibit distinctive multi-stage representational trajectories. (C) A quantitative analysis of the temporal evolution of feature selectivity reveals a staggered emergence of representational distinctions within and across ventral stream ROIs (black curve = V1-3, blue = V4t/LO, red = IT/PHC). Horizontal bars indicate time points with effects significantly exceeding pre-stimulus baseline (nonparametric cluster-correction; cluster inclusion and significance level  $p < 0.05$ ). Standard error across participants shown as shaded area. Representational geometries at selected time points and ROIs are reconstructed in 2D using multidimensional scaling (MDS) to visualize effect magnitude.

In order to test for bidirectional information transfer between ROIs, we performed bottom-up and top-down Granger-causality analysis. Granger causality is present when the past time course of a source explains significant additional variance in the target when added to a model already containing the target's past. We estimated the extra variance explained by the source ROI's past RDM movie (-120 ms to -20 ms) in the target ROI's present RDM when added to a linear model already containing the target ROI's past RDM movie (-120 ms to -20 ms). As expected, Granger causality was significant from V1-3 to V4t/LO and from V4t/LO to IT/PHC in the feedforward direction, emerging around 70 ms after stimulus onset in each case. Importantly, Granger causality was also significant in the feedback direction, emerging gradually with a peak just past 110 ms for V4t/LO to V1-3, and around 140 ms for IT/PHC to V4t/LO. Granger causality is model-dependent and the model did not include common input to source and target regions. However, the bidirectional significance is difficult to reconcile with input at differential delays from a third lower-level region.

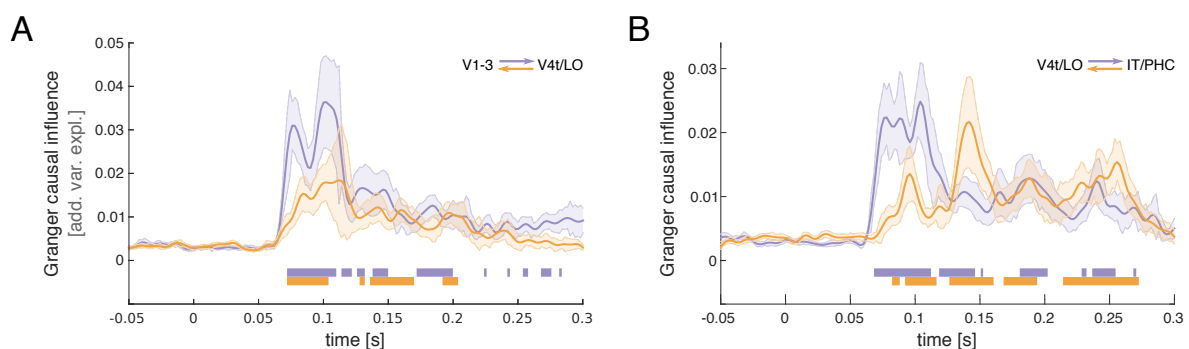


**Figure 2. RSA Granger causality analysis was performed to estimate information flow between ventral stream areas.** (A) Feedforward (purple) and feedback (orange) direction of Granger causal influence between early- and intermediate ROIs, and (B) effects between intermediate- and high-level ROIs. Horizontal bars indicate time points with causal interactions exceeding effects during pre-stimulus baseline (FDR corrected at  $q < 0.05$ ).

Our analyses thus far suggest a prominent role of recurrence in computations along the ventral visual pathway. We next explicitly tested this hypothesis with image-computable models of brain information processing<sup>27–30</sup>. We trained different deep neural network architectures to capture the time-varying representations across all ventral-stream areas (Figure 3A) and compared the models in terms of their ability to predict held-out MEG data. Two classes of convolutional neural network architecture were tested: recurrent and feedforward. The recurrent models included bottom-up, lateral, and top-down connections (BLT)<sup>6</sup>. All models were approximately matched in the number of parameters (see Methods for details). Pure feedforward architectures are severely limited with respect to the dynamics they can express. To maximize the potential for complex dynamics within the feedforward framework, we allowed units to ramp-up their activity over time. This was achieved via self-connections, whose weights were optimized along with the other parameters to best match the MEG data. Ramping feedforward models can exhibit complex dynamics, capturing for example the way neurons integrate incoming signals and accumulate evidence. While this technically constitutes a recurrent architecture, it does not enable lateral and top-down message passing. Ramping feedforward models include pure feedforward models as a special case and therefore provide a more conservative control in testing the hypothesis of recurrent computation in the ventral stream.

The networks were trained to match the human data by using the RDM movies of the three ventral-stream ROIs as deep-learning targets for separate network layers. We optimized each model to best predict the MEG RDM movies using backpropagation (representational distance learning (RDL)<sup>31</sup>, see Methods for training details). To avoid overfitting to the 92 experimental stimuli, a separate set of 141,000 images from the same categories was used for network training (Supplemental Figure 3). Each trained network was tested on the previously

unseen experimental stimuli, and the fit between the network RDM movies and the MEG RDM movies was estimated by cross-validation (see Supplemental Figure 4 and Supplemental Movie 2-6 for a direct comparison of model and ventral-stream RDM movies).

We first compared deep neural networks (DNNs) and MEG data in terms of the average representational distance across all stimulus pairs for each time point (Figure 3B). While ramping feedforward networks exhibit complex representational dynamics, their average representational distances did not closely follow the empirical data, especially in higher-level ventral-stream regions (average-distance trajectory correlations with held-out data: 0.83, 0.59, 0.47 for V1-3, V4t/LO, and IT/PHC, respectively). In contrast, recurrent DNNs almost perfectly matched the average distances of all ventral-stream ROIs (average-distance trajectory correlations: 0.95, 0.93, 0.97 for V1-3, V4t/LO, and IT/PHC, respectively; significantly outperforming ramping feedforward models for all ROIs and cross-validation splits at  $p < 0.0001$  using Hittner's  $r$  to  $z$  procedure<sup>32,33</sup>). Next, we evaluated how well the models matched the detailed patterns of representational distances in the RDM movies frame by frame. For each time point, we computed the correlation between the RDM of the corresponding model layer and the ventral-stream RDM. These correlations were averaged across time to yield a summary statistic (Figure 3C, see Supplemental Figure 5 for the full time-courses). For each ventral-stream area, the recurrent model significantly outperformed the ramping feedforward models (Wilcoxon signed-rank test,  $p < 0.005$  in all cases). The recurrent model, fitted to the time-varying MEG data, also significantly outperformed ramping feedforward models when tested on functional magnetic resonance imaging (fMRI) data acquired from the same participants (Figure 3D;  $p < 0.001$  for V1-3,  $p < 0.05$  for V4t-LO,  $p < 0.001$  for IT/PHC; see Methods and Supplementary Figure 6 for details). Finally, the recurrent architectures also outperformed the ramping feedforward models in terms of



classification performance on the held-out test set by a large margin (top-1 accuracy ~64% for the ramping feedforward models ( $B_{K9}$ ,  $B_{K11}$ ), and 73.9% for the recurrent models).

Our analyses of the RDM dynamics, Granger causality between regions, and DNN models all consistently show that human ventral-stream dynamics arise from recurrent message passing. The combination of source-based MEG representational dynamics analysis and recurrent deep neural network models opens new horizons for investigation of information processing in the human brain.

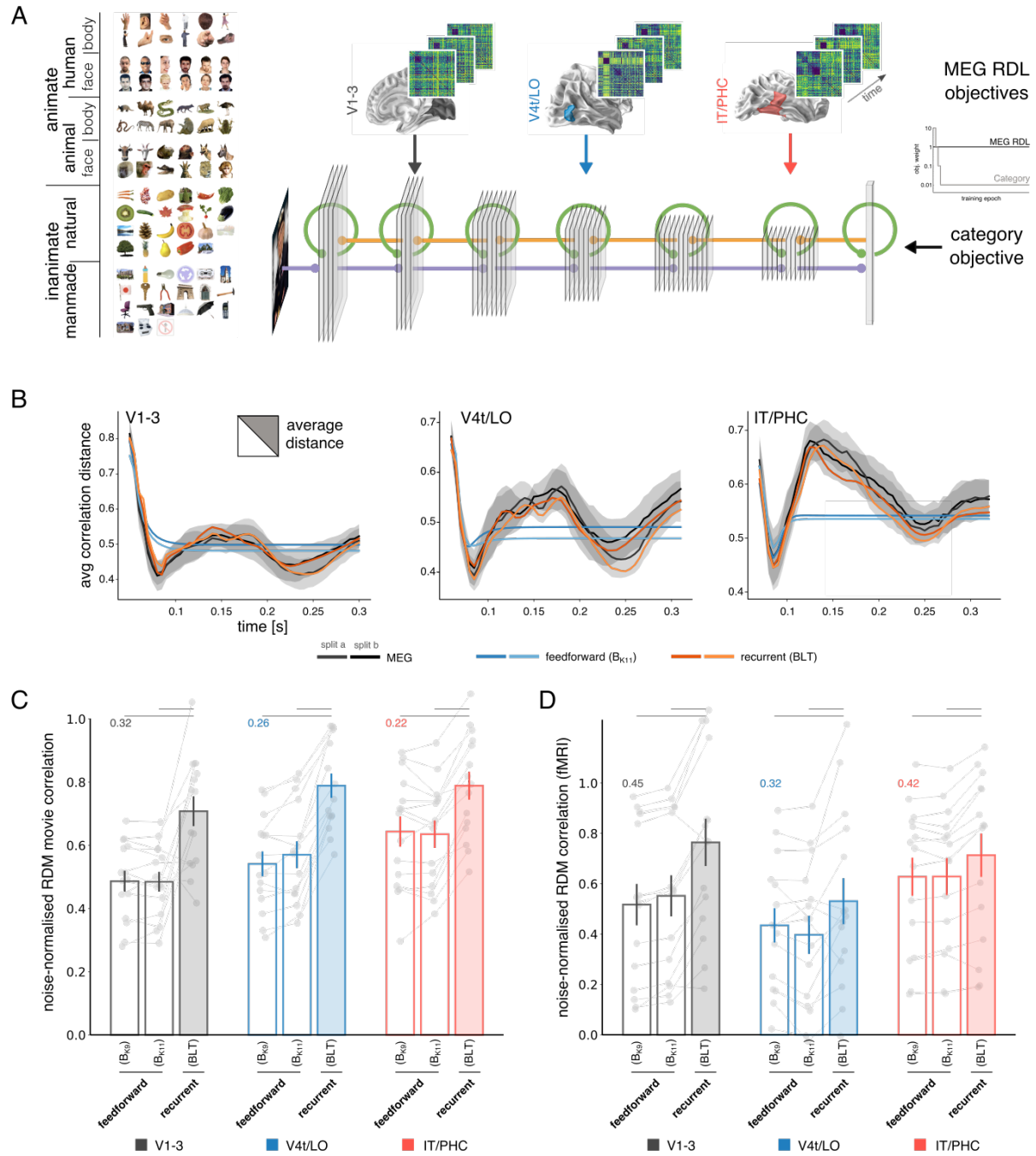


**Figure 3. Deep neural network modelling of ventral stream representational dynamics.** (A) The RDM movie of each ventral stream region was used as a time-varying deep learning target for a separate DNN layer. Each artificial network thereby attempts to simultaneously capture the representational dynamics of all ventral stream areas. (B) Development of the average pattern distance across time. MEG data are shown together with the results of ramping feedforward, and recurrent DNNs. (C) Average frame-by-frame RDM correlation between model and brain (correlations estimated on separate data from individual participants, data are normalized by the predictive performance of the MEG RDM movies used for training). For all ROIs (black = V1-3, blue = V4t/LO, red = IT/PHC), recurrent BLT networks significantly outperform ramping feedforward architectures. (D) Cross-validated predictive performance of different DNN architectures trained on the MEG

data when tested on fMRI RDMs acquired from the same participants. For all ROIs, recurrent networks significantly outperform ramping feedforward architectures.

## References

1. Grill-Spector, K. & Weiner, K. S. The functional architecture of the ventral temporal cortex and its role in categorization. *Nat. Rev. Neurosci.* **15**, 536–548 (2014).
2. Kravitz, D. J., Saleem, K. S., Baker, C. I., Ungerleider, L. G. & Mishkin, M. The ventral visual pathway: an expanded neural framework for the processing of object quality. *Trends Cogn. Sci.* **17**, 26–49 (2013).
3. Freiwald, W. A. & Tsao, D. Y. Functional compartmentalization and viewpoint generalization within the macaque face-processing system. *Science (80-. )*. **330**, 845–51 (2010).
4. Sugase, Y., Yamane, S., Ueno, S. & Kawano, K. Global and fine information coded by single neurons in the temporal visual cortex. *Nature* **400**, 869–73 (1999).
5. Nayebi, A. *et al.* Task-Driven Convolutional Recurrent Models of the Visual System. in *Advances in Neural Information Processing Systems 31* (eds. Bengio, S. *et al.*) 5295–5306 (Curran Associates, Inc., 2018).
6. Spoerer, C. J., McClure, P. & Kriegeskorte, N. Recurrent convolutional neural networks: a better model of biological object recognition under occlusion. *Front. Psychol.* **8**, 1–14 (2017).
7. Yau, J. M., Pasupathy, A., Brincat, S. L. & Connor, C. E. Curvature processing dynamics in macaque area V4. *Cereb. Cortex* **23**, 198–209 (2013).
8. Wyatte, D., Curran, T. & O'Reilly, R. The Limits of Feedforward Vision: Recurrent Processing Promotes Robust Object Recognition when Objects Are Degraded. *J. Cogn. Neurosci.* **24**, 2248–2261 (2012).
9. Li, Z., Yang, Y., Liu, X., Wen, S. & Xu, W. Dynamic Computational Time for Visual Attention. in *ICCV* 1–11 (2017).
10. Han, K. *et al.* Deep Predictive Coding Network with Local Recurrent Processing for Object Recognition. 1–12 (2018).
11. Tang, H. *et al.* Recurrent computations for visual pattern completion. *arXiv* (2018).
12. Wyatte, D., Jilk, D. J. & O'Reilly, R. C. Early recurrent feedback facilitates visual object recognition under challenging conditions. *Front. Psychol.* **5**, (2014).
13. Hupé, J. M. *et al.* Feedback connections act on the early part of the responses in monkey visual cortex. *J. Neurophysiol.* **85**, 134–145 (2001).
14. Kriegeskorte, N., Mur, M. & Bandettini, P. Representational similarity analysis - connecting the branches of systems neuroscience. *Front. Syst. Neurosci.* **2**, 4 (2008).
15. Haxby, J. V., Connolly, A. C. & Guntupalli, J. S. Decoding Neural Representational Spaces Using Multivariate Pattern Analysis. *Annu. Rev. Neurosci.* **37**, 435–456 (2014).
16. Glasser, M. F. *et al.* A multi-modal parcellation of human cerebral cortex. *Nature* **536**, 171–8 (2016).
17. Cichy, R. M., Pantazis, D. & Oliva, A. Resolving human object recognition in space and time. *Nat. Neurosci.* **17**, 455–462 (2014).
18. Hämläinen, M. & Ilmoniemi, R. Interpreting magnetic fields of the brain: minimum norm estimates. *Med. Biol. Eng. Comput.* **32**, 35–42 (1994).
19. Oliva, A. *et al.* Building the Gist of a Scene: The Role of Global Image Features in Recognition. *Prog. Brain Res.* **155**, Part, 2005–2008 (2008).
20. Kriegeskorte, N. *et al.* Matching Categorical Object Representations in Inferior Temporal Cortex of Man and Monkey. *Neuron* **60**, 1–16 (2008).
21. Konkle, T. & Caramazza, A. Tripartite Organization of the Ventral Stream by Animacy and Object Size. *J. Neurosci.* **33**, 10235–10242 (2013).
22. Bell, A. H., Hadj-Bouziane, F., Frihauf, J. B., Tootell, R. B. H. & Ungerleider, L. G. Object representations in the temporal cortex of monkeys and humans as revealed by

- functional magnetic resonance imaging. *J. Neurophysiol.* **101**, 688 (2009).
23. Konkle, T. & Oliva, A. A Real-World Size Organization of Object Responses in Occipitotemporal Cortex. *Neuron* **74**, 1114–1124 (2012).
  24. Kanwisher, N. & Yovel, G. The Fusiform Face Area: A Cortical Region Specialized for the Perception of Faces. *Philos. Trans. R. Soc. B Biol. Sci.* **361**, 2109 (2006).
  25. Khaligh-Razavi, S.-M. & Kriegeskorte, N. Deep Supervised, but Not Unsupervised, Models May Explain IT Cortical Representation. *PLoS Comput. Biol.* **10**, 1–29 (2014).
  26. Kiani, R., Esteky, H., Mirpour, K. & Tanaka, K. Object category structure in response patterns of neuronal population in monkey inferior temporal cortex. *J. Neurophysiol.* **97**, 4296–309 (2007).
  27. Kietzmann, T. C., McClure, P. & Kriegeskorte, N. Deep Neural Networks In Computational Neuroscience. *Oxford Res. Encycl. Neurosci.* 1–28 (2019). doi:10.1101/133504
  28. Kriegeskorte, N. Deep neural networks: a new framework for modelling biological vision and brain information processing. *Annu. Rev. Vis. Sci.* **1**, 417–446 (2015).
  29. Yamins, D. L. & DiCarlo, J. J. Using goal-driven deep learning models to understand sensory cortex. *Nat. Neurosci.* **19**, 356–365 (2016).
  30. Kumbhani, J. *et al.* CORnet : Modeling the Neural Mechanisms of Core Object Recognition. 1–9 (2018). doi:10.1101/408385
  31. McClure, P. & Kriegeskorte, N. Representational Distance Learning for Deep Neural Networks. *Front. Comput. Neurosci.* **10**, 131 (2016).
  32. Hittner, J. B., May, K. & Silver, N. C. A monte carlo evaluation of tests for comparing dependent correlations. *J. Gen. Psychol.* **130**, 149–168 (2003).
  33. Diedenhofen, B. & Musch, J. Cocor: A comprehensive solution for the statistical comparison of correlations. *PLoS One* **10**, 1–12 (2015).

**Acknowledgments.** This research was funded by the UK Medical Research Council (Programme MC-A060- 5PR20), by a European Research Council Starting Grant (ERC-2010-StG 261352), by the Human Brain Project (EU grant 604102), and a DFG research fellowship to TCK.

**Author Contributions.** Conceptualization: TCK, NK; Methodology: TCK, CS, OH, NK; Formal Analysis: TCK, CS, LS; Investigation: TCK, RC, CS, LS; Writing - Original Draft: TCK, CS, NK; Writing – Review and Editing: TCK, CS, LS, RC, OH, NK; Funding Acquisition: NK, RC, TCK, LS

**Competing interests.** The authors declare no competing interests.

**Supplementary Materials:**

Materials and Methods

Figures S1-S7

Tables S1

Movies S1-S6

## **Supplementary Materials and Methods**

### **MEG data acquisition, pre-processing and source reconstruction**

#### **Experimental setup**

Data collection procedures and experimental design were described in detail previously<sup>17</sup>. MEG data from 16 right-handed participants (10 females, mean age 25.87 years; std = 5.38) were recorded. MEG source reconstruction analyses were performed for a subset of 15 participants for whom additional structural and functional MRI data were acquired. All participants had normal or corrected-to-normal vision and gave written informed consent in each experimental session (two MEG, 1 fMRI for each participant). The study was approved by the Institutional Review Board of the Massachusetts Institute of Technology and conducted according to the Declaration of Helsinki.

During the experiment, participants were shown 92 different objects. This stimulus set was used across multiple studies and laboratories to collect human fMRI<sup>20</sup>, and MEG data<sup>17,34</sup>, human perceptual similarity judgments<sup>35</sup>, macaque single cell data<sup>26</sup>, and was used in previous investigations of deep neural network models<sup>25,36</sup>. The stimulus set therefore allows for comparisons across modalities, species, and recording sites. Furthermore, it includes a large variety of object categories, allowing for a more complete characterization of population responses in the human visual cortex, compared to less diverse sets. It includes depictions of 12 human body parts, 12 human faces, 12 animal bodies, 12 animal heads, 23 natural objects, and 21 artificial/manmade objects.

Each participant completed two experimental MEG sessions. Stimuli were presented on a grey background (2.9 degrees of visual angle, 500 ms stimulus duration), overlaid with a dark grey fixation cross (trial onset asynchrony (TOA) of 1.5 or 2 s). Participants were asked to indicate via button press and eye blink whenever they noticed the appearance of a paper clip. These target trials, occurring randomly every 3-5 trials, were excluded from further analyses. Each session consisted of 10-14 runs, and each stimulus was presented twice in a given run.

#### **MEG data acquisition and pre-processing**

Data were acquired from 306 MEG channels (102 magnetometers, 204 planar gradiometers) using an Elekta Neuromag TRIUX system (Elekta, Stockholm). The raw data, sampled at 1 kHz, were bandpass filtered between 0.03 and 330Hz, cleaned using spatiotemporal filtering (maxfilter software, Elekta, Stockholm), and subsequently downsampled to 500Hz. Trials were baseline-corrected using a time-window of 100 ms before stimulus onset. For each participant and session, flat sensors and sensors exhibiting excessive noise (defined as baseline variance exceeding a z-threshold of  $\pm 3$ , z-scores computed over the distribution of all sensors of a given type) were removed from further analyses. On average, 2.67 gradiometers ( $std = 1.79$ ) and 0.67 magnetometers ( $std = 1.06$ ) were excluded. Trials with excessive noise were discarded by means of the autoreject toolbox<sup>37</sup>. After cleaning, an average of 26.08 (range 16 - 35) repetitions per stimulus, participant, and session entered subsequent analyses.

## MEG source reconstruction

### *Source reconstructions*

Source reconstructions were performed using MNE<sup>18</sup>, as implemented in the MNE python toolbox<sup>38</sup>. Volume conduction estimates were based on participant individual structural T1 scans, using single layer boundary element models (BEMs). BEMs were based on the inner skull boundary (extracted via fieldtrip<sup>39</sup> due to poor reconstruction results from the FreeSurfer<sup>40</sup> watershed algorithm used in MNE python). The source space comprised 10242 source points per hemisphere, positioned along the grey/white boundary, as estimated via FreeSurfer. Source orientations were defined as surface normals with a loose orientation constraint. MEG/MRI alignment was performed based on fiducials and digitizer points along the head surface (iterative closest point procedure after initial alignment based on fiducials). The sensor noise covariance matrix was estimated from the baseline period (-0.1 – 0 s with respect to stimulus onset) and regularized according to the Ledoit-Wolf procedure<sup>41</sup>. Source activations were projected onto the surface normal, yielding one activation estimate per point in source space and time.

### *Regions of interest*

Three regions of interest (ROIs) were defined along the ventral visual stream, covering early (V1-3), intermediate (V4t/LO1-3) and downstream, high-level visual areas (IT/PHC, consisting of TE1-2p, FFC, VVC, VMV2-3, PHA1-3). ROIs were defined comparably large and spatially distinct to maximize SNR while limiting cross-talk. A potential separation of the early ROI into multiple smaller visual areas is complicated by the small stimulus size (2.9 degree visual angle), preventing a clear attribution of activity near the foveal confluence.

Each ROI was derived from a multi-modal atlas of cerebral cortex, which provides the underlying parcellation<sup>16</sup>. The atlas annotation files were converted to fsaverage coordinates<sup>42</sup> and from there mapped to each individual participant via spherical averaging.

## **MEG Representational dynamics analysis**

We used representational similarity analysis (RSA)<sup>14</sup> to gain insights into the representational transformations of the visual inputs across time for all three regions of interest. The central element of RSA are representational dissimilarity matrices (RDMs), which characterize how a given ROI distinguishes between experimental conditions. A small distance between a pair of conditions implies a similar neural response, whereas large distances imply that the region treats the two stimulus conditions separately. RDMs thereby equate to representational geometries, which define the spatial relationship of experimental conditions in the underlying activation space. To get a better understanding of the organizational principles underlying a given RDM, computational and categorical models can be used to predict (condition relative) empirical distances. Temporal sequences of RDMs across multiple ROIs can furthermore be used to test for effects of granger causality; i.e. the transfer of representational organizations between ROIs.



## **RDM extraction**

To compute temporally resolved RDM movies from MEG source data, we first extracted a single multivariate source time-series for each condition by averaging across repetitions. RDMs were then computed by estimating the pattern distance between all combinations of conditions using correlation distance (1-Pearson correlation). One RDM was computed for each time point, yielding a temporally changing RDM movie (size:  $n\_objects \times n\_objects \times n\_timepoints$ ). RDM movies were computed for each participant, ROI, hemisphere, and session separately. We then averaged the RDM movies across hemispheres and sessions, yielding one RDM movie for each ROI and participant. As RDMs are diagonally symmetric, only the upper triangles of the RDM movies were used for subsequent analyses. For visualization purposes, all shown RDMs are rank-transformed. All analyses were performed on the non-transformed data.

## **Model fitting and statistics**

To better understand and quantitatively assess representational transformations across time, we modelled the RDM movies of each participant and ROI using a hierarchical GLM. The overall idea of RDM modelling is to define a set of external computational/categorical models, each predicting distinct condition-specific distances, which are then combined to explain the observed empirical distances. These predictors are not necessarily orthogonal, and therefore the actual contribution of each predictor to the overall variance explained can be ambiguous. To solve this issue, we here compute unique variance explained of each model predictor by subtracting the total variance explained of the reduced GLM (excluding the predictor of interest) from the total variance explained by the full GLM. This procedure was followed for each model predictor, participant, ROI, and time-point.

To find the optimal weights for the linear combination of model predictors, we used a non-negative least squares approach. The predictions of four main and 10 additional control predictors were investigated. The resulting fourteen model predictors were standardized before entering the GLM. The main predictors included animate-, and face-clustering, low-level GIST predictions, and representational geometries resulting from organizations based on the real-world size<sup>23</sup>. Beyond these four, additional predictors were included, which mirror the categorical structure of the stimulus space: inanimate-, human-, animal-, face-(monkey, inter-species), body (human, monkey), natural- and artificial object clustering. Finally, a constant term was included in the GLM model. Following the GLM modelling approach described above, we obtained unique variance traces across time for each participant, GLM predictor and ROI. Predictor-specific statistical tests were performed across participants for each ROI and time-point.

To establish whether the unique variance explained by a model predictor exceeded the expected increase due to the addition of a free parameter to the GLM, we tested the unique variance observed at each time point against the average increase during the pre-stimulus baseline period. To control for multiple comparisons across time, a non-parametric cluster test was used max-sum test statistic, computed on a paired, one-sided t-statistic (one-sided because effects of interest are strictly larger than the effects observed during baseline); cluster inclusion criterion of  $p < 0.05$ )<sup>43</sup>. The statistical baseline period was defined as the 50 ms time-window directly prior to stimulus onset. The first 600 ms of stimulus processing

were included in the analyses. Statistical comparisons were performed on the unsmoothed signal. To aid visibility, unique variance curves were low-pass filtered at 80 Hz (Butterworth IIR filter; order 6) prior to plotting.

### **RSA Granger analysis**

To investigate the possibility of information transfer between ROIs, we performed a Granger causality analysis on the basis of the RDM movies<sup>44</sup>. That is, we asked whether the current RDM of a target ROI could be explained by the past RDMs of a source ROI, beyond the explanation offered by the past of the target ROI itself. As for the model predictions above, this was also implemented by a hierarchical GLM approach (again using non-negative least squares). We first used the past RDMs of the target ROI itself to explain the current RDM, and then tested in how far the addition of the past RDMs from a source RDM would add to the variance explained. Again, the inclusion of additional predictors, and therefore free parameters, can by itself lead to an increase in the variance explained. We therefore used the average increase in variance explained during a pre-stimulus time window (50 ms prior to stimulus onset) as baseline for statistical comparisons. For each pair of adjacent ROIs (V1-3 and V4t/LO1-3, as well as V4t/LO1-3 and IT/PHC), we tested both directions of Granger causality, using the standardized RDMs of each ROI once as source and once as target. To predict the RDM data at time point  $t$ , we used a 100 ms time-window of  $t-120$  ms to  $t-20$  ms. To test for effects of Granger causality across time, we performed above analysis separately for each time-point within the first 300 ms post stimulus onset. To correct for multiple comparisons, we performed an FDR correction ( $p < 0.05$ ) for all tested time-points tested for the two source ROIs. Statistical comparisons were performed on the unsmoothed signal. To aid visibility, unique variance curves were low-pass filtered at 80 Hz (Butterworth IIR filter; order 6) prior to plotting.

## **FMRI data acquisition and analyses**

FMRI data were collected for 15 participants. Stimuli were presented once per run, participants completed between 10 and 14 runs each. Each run contained additional 30 randomly timed null trials without stimulus presentation. During these trials, participants had the task to report a short (100ms) change in the luminance of the fixation cross via button-press. fMRI experimental trials had a TOA of 3 seconds (6 s in presence of a null trial). For further acquisition details, please see <sup>17</sup>. Pre-processing was performed using SPM8 (<http://www.fil.ion.ucl.ac.uk/spm/>). Functional data were spatially realigned, slice-time corrected and co-registered to the participant-individual T1 structural image. Data were then modelled using a general linear model (GLM), which included movement parameters as nuisance terms. GLM parameter estimates for each condition/stimulus were contrasted against an explicit baseline to yield a t-value for each voxel and condition. The 500 most strongly activated voxels were included in subsequent analyses.

Regions of interest were defined in alignment with the MEG ROIs. The corresponding ROI masks were defined on the individual surface and projected into the functional volume using freesurfer<sup>40</sup>. To characterize the representational geometry of a given ROI, the activation patterns (t-values) were extracted for all possible pairs of stimuli, and the pattern distances were computed based on 1-Pearson correlation, in line with the distance measures used in the MEG data.

## **RCNN model predictions of fMRI data**

RCNN models, originally fitted to the MEG data, were used to predict the temporally smooth fMRI representational similarities. Since the RCNN models predict temporal sequences of RDMs for each ROI, the time-points of a given layer were linearly combined to obtain a single RDM prediction for the fMRI data. Network layers were chosen for each fMRI ROI to match the corresponding MEG ROI used during training.

The linear weights for the individual time-points were computed using non-negative least-squares, fitting to the average RDM of a given ROI based on the data of N-1 participants. The resulting reconstruction was then used to predict the RDM of the left-out participant. The goodness of fit of this cross-validated prediction was determined by correlating the upper triangles of the two RDMs. Prediction accuracies were statistically compared using random effects test across participants (non-parametric Wilcoxon signed rank test).

## **Neural network models**

We modelled the observed MEG RDM movies with convolutional neural networks implemented using TensorFlow<sup>45</sup>. Two specific architectures were tested, feedforward networks, where bottom-up connections dominate (termed ‘B’ for bottom-up hereafter), and a recurrent network, with bottom-up, lateral and top-down connections (BLT)<sup>6</sup>. Feedforward and recurrent models were matched to have approximately the same number of parameters. To enable feedforward networks to exhibit non-trivial dynamics, we allowed the networks to learn to ramp-up the activity of their units over time.

### **Training data sets**

Networks were trained using representational distance learning (RDL)<sup>31</sup> to predict the time-varying representational dynamics in the ventral stream up to 300ms after stimulus onset. To train the networks with RDL we collected a data set of 141,000 images – RDL61. This data set consists of 61 categories derived from the 92 images that were used in the human imaging experiments. For each category in the experimental stimulus set, a set of natural images were obtained and subdivided into a training set and a validation set.

### **Image pre-processing**

During network training, each image underwent a series of pre-processing steps before being passed to the network. Firstly, a crop was randomly sampled from the image that covered at least a third of the of the image area with an aspect ratio in the range 0.9-1.1 (specified as the ratio width/height). The image was then randomly flipped along the vertical axis, and small random distortions were applied to the brightness, saturation and contrast. Finally, the image was resized to 96×96 pixels.

### **Cross-validation**

To avoid overfitting, we cross-validated the networks with respect to both, the input images and the MEG data. Firstly, all of the network responses were analyzed using the same 92 stimuli that were shown to the human participants. These images are both independent and visually dissimilar (showing only a single object on a grey background) from the natural images used to train the networks.

Secondly, networks were evaluated against MEG data that was held out from the model fitting procedure. This was accomplished by assigning single-session data for each subject to one of two splits. Networks were always tested using the split of the data that was not used during training. We used a two-fold cross-validation procedure due to the excessive time taken to train the networks. To ensure that cross-validation was representative of the data, despite the small number of folds, the distribution of split-half reliabilities of all possible splits was computed and the split that best represented the mean of the distribution was chosen for all further analyses.

## Architectural overview

Each network contains six convolutional layers followed by a linear readout. All convolutions have a stride of  $1 \times 1$  and are padded such that the convolution leaves the height and width dimensions of the layer unchanged. Prior to each convolutional layer (except the first), the feedforward input to the network goes through a max pooling layer with  $2 \times 2$  stride and a  $2 \times 2$  kernel. This has the effect of reducing the height and width dimensions of the input by a factor of 2.

Architectural parameters are outlined in Supplementary Table 1 including the number of feature maps, kernel size and image size for each layer. The addition of lateral and top-down connections in BLT leads to an increased number of parameters compared to a feedforward B model. A larger kernel size is used in B to approximately match the number of parameters in BLT, while maintaining the same number of units and layers across the networks. As it is not possible to exactly match the number of parameters by adjusting the kernel size, we use the two closest B models, with kernel sizes of 9 and 11, subsequently referred to as  $B_{K9}$  and  $B_{K11}$ , respectively.

For architectural simplicity, the kernel size was kept fixed throughout the networks. If the image size reduces to less than  $(k + 1)/2$  (where  $k$  is an odd kernel size), then the whole kernel is not used after it has been centred on each of the inputs. This reduces the effective kernel size for the layer, which only occurs in the final convolutional layer of B (see Supplementary Table 1). Taking the effective kernel size into account, the number of parameters sums to 3.0 million in  $B_{K9}$ , 4.3 million in  $B_{K11}$  and 4.0 million in BLT. Time is modelled in the neural networks by defining each convolution as taking a single time step. In practice, it is easier to implement the feedforward connections as instantaneous, lateral connections as taking one time step and top-down connections as taking two time steps. These two definitions are computationally equivalent if lateral and top-down connections have no influence prior to the arrival of feedforward input to the layer.

## Recurrent convolutional layers

The recurrent convolutional layer (RCL) forms the basis of the models used in these experiments. The activation in a single RCL is represented by the three-dimensional array  $H_{\tau,n}$ , the index  $\tau$  is used to indicate the time step and  $n$  is used to indicate the layer. The dimensions in  $H_{\tau,n}$  correspond to the height, width and features in the layer. We define  $H_{\tau,0}$  to be the input image to the network.

Convolutional weights for a given layer in the network are represented by the arrays  $W_n$ . All instances of  $W_n$  are implemented using weight normalisation to assist learning<sup>46</sup>. The biases for each layer are represented by the vector  $\mathbf{b}_n$ , with a unique bias for each feature map in the output.

For classic feedforward (B) networks, the lack of recurrent connections reduces RCLs to a standard convolutional layer

$$H_{\tau,n} = [W_n^b * H_{\tau-1,n-1} + \mathbf{b}_n]_+$$

Where  $W_n^b$  represents the bottom-up convolutional weights and  $[\cdot]_+$  is the rectified linear function. All layers are made inactive prior to the arrival of feedforward input to the layer by defining  $H_{\tau,n} = 0$  when  $\tau < n$ .

As standard feedforward networks lack dynamics, we modify the B layers to allow units to ramp-up their activation over time via self-connections. Self-connection weights are controlled by the parameter  $\omega_n$ , which is shared across the layer. Note that this model class contains conventional feedforward models as a special case, where  $\omega_n = 0$ . The self-connection weights were constrained to be nonnegative and optimized along with the other connection weights.

$$H_{\tau,n} = [W_n^b * H_{\tau-1,n-1} + \omega_n H_{\tau-1,n} + \mathbf{b}_n]_+$$

BLT layers are formed by the addition of lateral and top-down convolutions with weights  $W_n^l$  and  $W_n^t$ , respectively.

$$H_{\tau,n} = [W_n^b * H_{\tau-1,n-1} + W_n^l * H_{\tau-1,n} + W_n^t * H_{\tau-1,n+1} + \mathbf{b}_n]_+$$

Max-pooling has the effect of reducing the height and width dimensions of RCLs as we move up the layers of the network. This means that the size of the outputs from top-down convolutions does not match the size of the outputs for bottom-up and lateral convolutions, as the convolutions preserve image size. To compensate for this, we apply nearest-neighbor up-sampling to the output of the top-down convolution to make the sizes match. This has the effect of small, non-overlapping patches of neighboring units receiving identical top-down input.

In the final BLT layer, top-down input is drawn from the readout layer of the network. In this case, a fully connected layer is used for top-down connections as opposed to the convolutional layer that is used elsewhere.

## Readout layer

A linear readout is added to the end of the network to produce an output,  $\mathbf{h}_{\tau,\text{cat}}$ , for each of categories that the network is trained on.

Prior to the readout, the bottom-up input goes through global average pooling. This averages over the spatial dimensions of final layer,  $N$ , to produce a vector with length equal to the number of features in the final layer, which we denote  $\bar{\mathbf{h}}_{\tau-1,N}$ .

The readout layer is also provided with lateral input from the readout on the previous time step,  $\mathbf{h}_{\tau-1,\text{cat}}$ . This allows the network to sustain categorisation responses without depending on continuous bottom-up input.

In B networks, lateral inputs take the form of self-connections that enable the units to increase their activation over time, in the same manner as the B convolutional layers.

$$\mathbf{h}_{\tau,\text{cat}} = W_{\text{cat}}^b \bar{\mathbf{h}}_{\tau-1,N} + \omega_{\text{cat}} \mathbf{h}_{\tau-1,\text{cat}} + \mathbf{b}_{\text{cat}}$$

Where  $W_{\text{cat}}^b$  are fully-connected bottom-up weights.

In BLT networks, the readout units have a set of fully connected lateral weights,  $W_{\text{cat}}^l$ , so each readout unit receives input from all other readout units.

$$\mathbf{h}_{\tau,\text{cat}} = W_{\text{cat}}^b \bar{\mathbf{h}}_{\tau-1,N} + W_{\text{cat}}^l \mathbf{h}_{\tau-1,\text{cat}} + \mathbf{b}_{\text{cat}}$$

## Training

The networks were trained using a two objectives, representational distance learning and object classification.

### *Representational distance learning*

We extended representational distance learning<sup>31</sup> to be used as an objective which aims to match network representational dynamics across multiple selected layers to the RDM movies of three ventral stream regions. Input images were taken from the RDL61 image set, which matches the categorical structure of the experimental stimuli. We use RDL to train layers 2, 4 and 6 of the network to match the dynamics of V1-3, V4t/LO, and IT/PHC, respectively.

The ventral stream RDMs undergo several pre-processing steps before being used for RDL. First, distances are averaged across any of the 92 images that fall into the same category in RDL61. For instance, the 92 stimuli contain 12 images of faces that constitute a single category in RDL61. Since optimization was performed at the category level, a single distance estimate was obtained as the average across all face distances. Averaging distances over categories produces a  $61 \times 61$  RDM for each time point in the MEG data. Each of the reduced RDMs are down-sampled from 500Hz to 200Hz by taking average RDMs over 5ms time windows centred at 5ms intervals from  $t_{\text{start}}$  to  $t_{\text{start}} + 250\text{ms}$ . The value of  $t_{\text{start}}$  varies for each of the ROIs, for V1-3  $t_{\text{start}} = 50\text{ms}$ , for V4t/LO  $t_{\text{start}} = 60\text{ms}$ , and for IT/PHC  $t_{\text{start}} = 70\text{ms}$ . The delay between each of the ROIs was used to account for the time taken to perform feedforward processing, as the model does not process information prior to arrival of feedforward input.

To apply RDL, mini-batches are divided into  $M/2$  pairs, where  $M$  is the batch size. Images in the mini-batch are pseudo-randomly sampled so that each pair contains two images,  $x_a$  and  $x_b$ , from two different categories, category  $a$  and category  $b$ . Within a pair we calculate the correlation distance between the network activations in a given layer in response to these two images,  $\hat{d}_{\tau,n}(x_a, x_b)$ . This was performed for each time point and layer where RDL is applied. To compute the error for RDL, we compare  $\hat{d}_{\tau,n}(x_a, x_b)$  to the distance for the two categories in the ventral stream MEG data,  $d_{\tau,r}(a, b)$ .

$$E_{\text{RDL}} = \sum_{n \in L, r \in R} \frac{1}{T} \sum_{\tau} \frac{\left( \hat{d}_{\tau,n}(x_a, x_b) - d_{\tau,r}(a, b) \right)^2}{\sigma_{\tau,r}^2}$$

Where  $L = \{2, 4, 6\}$  represents the network layers where RDL is applied and  $r$  represents the corresponding ROI from the set of all ROIs,  $R$ , that were used in training. We use the

variance of the empirical RDM at each time step,  $\sigma_{\tau,r}^2$ , as a normalisation factor. This normalisation prevents the loss from being biased towards time points with larger variance in the RDMs. As a result, each time-point will impact the optimization independently of the RDM variance/noise level.

### *Categorization objective*

The loss for categorization is calculated in two stages. Firstly, the softmax output  $\hat{y}_{\tau,i}$  is computed from the readout layer of the network for every category and time point. The error for the categorization objective,  $E_{\text{cat}}$ , is computed by calculating the cross-entropy between the softmax output and target for each category output  $y_i$  (where the target category is represented with one-hot encoding) and then averaging across time.

$$E_{\text{cat}} = -\frac{1}{T} \sum_{t=1}^T \sum_{i=1}^C y_i \cdot \log \hat{y}_{\tau,i}$$

Where  $C$  represents the number of categories used during training and  $T$  is the total number of time steps.

### *Overall objective*

A combination of the RDL and categorization objectives, with additional L2-regularisation, produces the overall loss function for the network.

$$\mathcal{L} = \gamma_{\text{cat}} \bar{E}_{\text{cat}} + \gamma_{\text{RDL}} \bar{E}_{\text{RDL}} + \lambda \|\mathbf{w}\|_2$$

Where  $\bar{E}_{\text{cat}}$  and  $\bar{E}_{\text{RDL}}$  are the average of  $E_{\text{cat}}$  and  $E_{\text{RDL}}$  over the mini-batch. The contribution of each objective is controlled by the two coefficients  $\gamma_{\text{cat}}$  and  $\gamma_{\text{RDL}}$ . The level of L2-regularization is controlled by the coefficient  $\lambda = 10^{-5}$ , and  $\mathbf{w}$  represents all weights of the network in vectorised format.

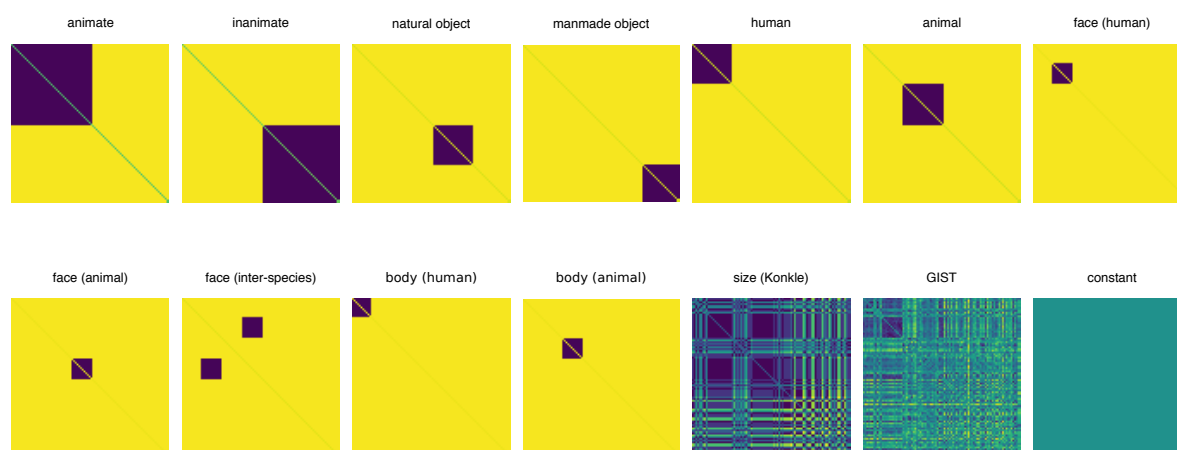
We set  $\gamma_{\text{RDL}} = 1$  throughout training, and initially set,  $\gamma_{\text{cat}} = 10$ , which causes the categorization loss to dominate at the beginning of training. Over the course of training  $\gamma_{\text{cat}}$  decays by a factor of 10 every 10,000 mini-batches until it reaches a value of  $10^{-2}$ , where it remains constant until training terminates after 4 million mini-batches.

We use Adam<sup>47</sup> to optimize the overall loss with the following parameters, learning rate  $\alpha = 10^{-3}$ , exponential decay parameters  $\beta_1 = 0.9$  and  $\beta_2 = 0.999$ , and stabilisation parameter  $\hat{\epsilon} = 10^{-1}$ . See Supplementary Figure 7 for image classification test performance across training for the different model types.

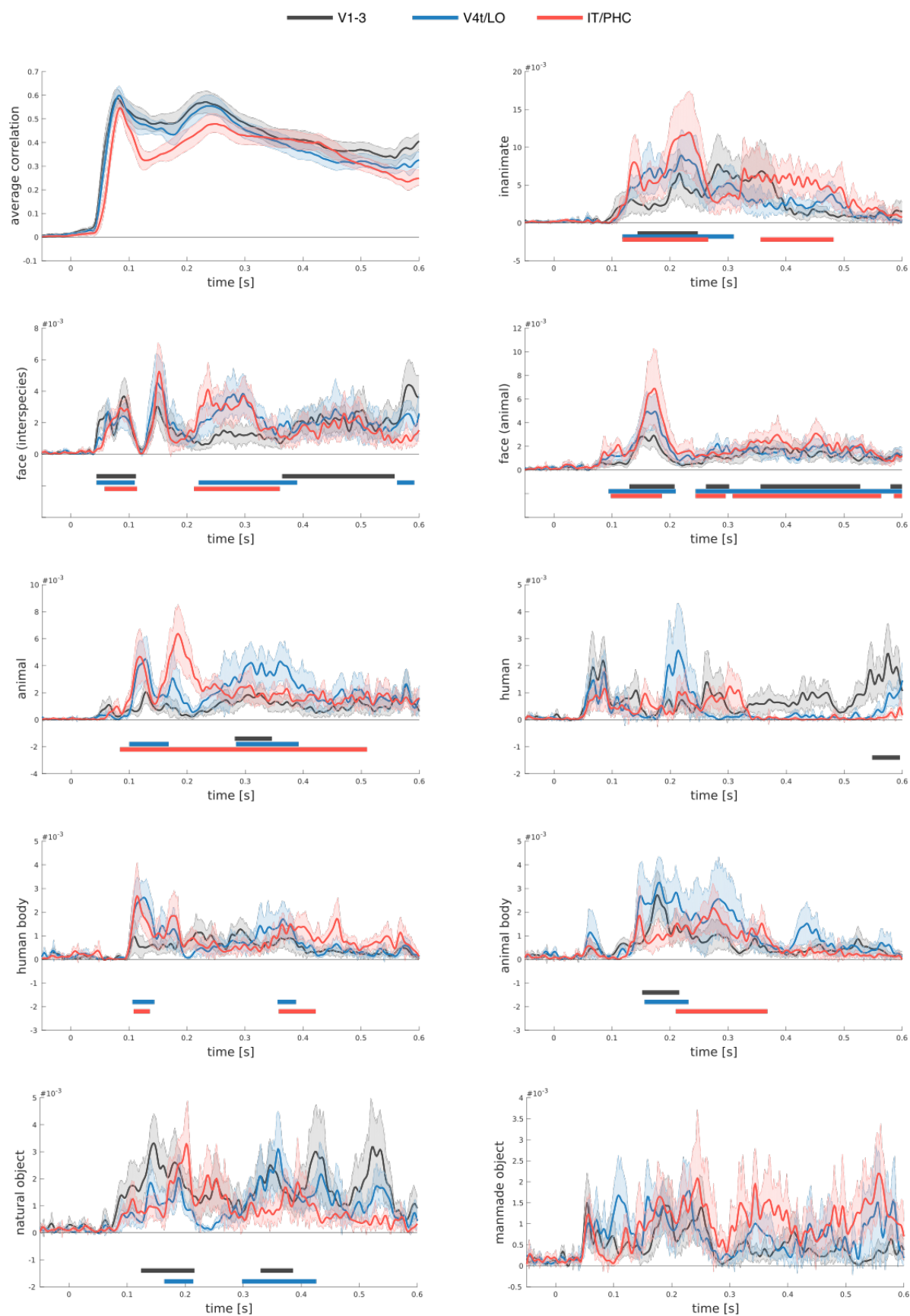


## References Supplementary

34. Carlson, T., Tovar, D., Alink, A. & Kriegeskorte, N. Representational dynamics of object vision: The first 1000 ms. *J. Vis.* **13**, 1–19 (2013).
35. Mur, M. *et al.* Human object-similarity judgments reflect and transcend the primate-IT object representation. *Front. Psychol.* **4**, 1–22 (2013).
36. Mehrer, J., Kietzmann, T. C. & Kriegeskorte, N. Deep neural networks trained on ecologically relevant categories better explain human IT. in *Cognitive Computational Neuroscience Meeting* **1**, 1–2 (2017).
37. Jas, M., Engemann, D. A., Bekhti, Y., Raimondo, F. & Gramfort, A. Autoreject: Automated artifact rejection for MEG and EEG data. *Neuroimage* **159**, 417–429 (2017).
38. Gramfort, A. *et al.* MEG and EEG data analysis with MNE-Python. **7**, 1–13 (2013).
39. Oostenveld, R., Fries, P., Maris, E. & Schoffelen, J.-M. FieldTrip: Open source software for advanced analysis of MEG, EEG, and invasive electrophysiological data. *Comput. Intell. Neurosci.* **2011**, 1–10 (2011).
40. Dale, A. M., Fischl, B. R. & Sereno, M. I. Cortical surface-based analysis. I. Segmentation and Surface Reconstruction. *Neuroimage* **9**, 179–194 (1999).
41. Ledoit, O. & Wolf, M. A well-conditioned estimator for large-dimensional covariance matrices. *J. Multivar. Anal.* **88**, 365–411 (2004).
42. Fischl, B. R., Sereno, M. I., Tootell, R. B. & Dale, A. M. High-resolution intersubject averaging and a coordinate system for the cortical surface. *Hum. Brain Mapp.* **8**, 272–84 (1999).
43. Maris, E. & Oostenveld, R. Nonparametric statistical testing of EEG- and MEG-data. *J. Neurosci. Methods* **164**, 177–90 (2007).
44. Goddard, E., Carlson, T. A., Dermody, N. & Woolgar, A. Representational dynamics of object recognition : Feedforward and feedback information flows. *Neuroimage* **128**, 385–397 (2016).
45. Abadi, M. *et al.* TensorFlow: A System for Large-Scale Machine Learning. in *OSDI* **16**, 265–283 (2016).
46. Salimans, T. & Kingma, D. P. Weight normalization: A simple reparameterization to accelerate training of deep neural networks. in *Advances in Neural Information Processing Systems* 901–909 (2016).
47. Kingma, D. P. & Ba, J. L. Adam: A Method for Stochastic Optimization. in *International Conference on Learning Representations* (2015).



**Supplemental Figure 1.** RDM components used as predictors during hierarchical GLM modelling. The overall GLM included 11 categorical predictors, as well as a predictor derived from low-level Gist features, real-world size, and a constant.



**Supplemental Figure 2.** Supplemental results of the hierarchical GLM model fitting procedure. Top left: average pattern distance across time for the three ventral stream ROIs. All others: unique variance explained by all control model predictors.

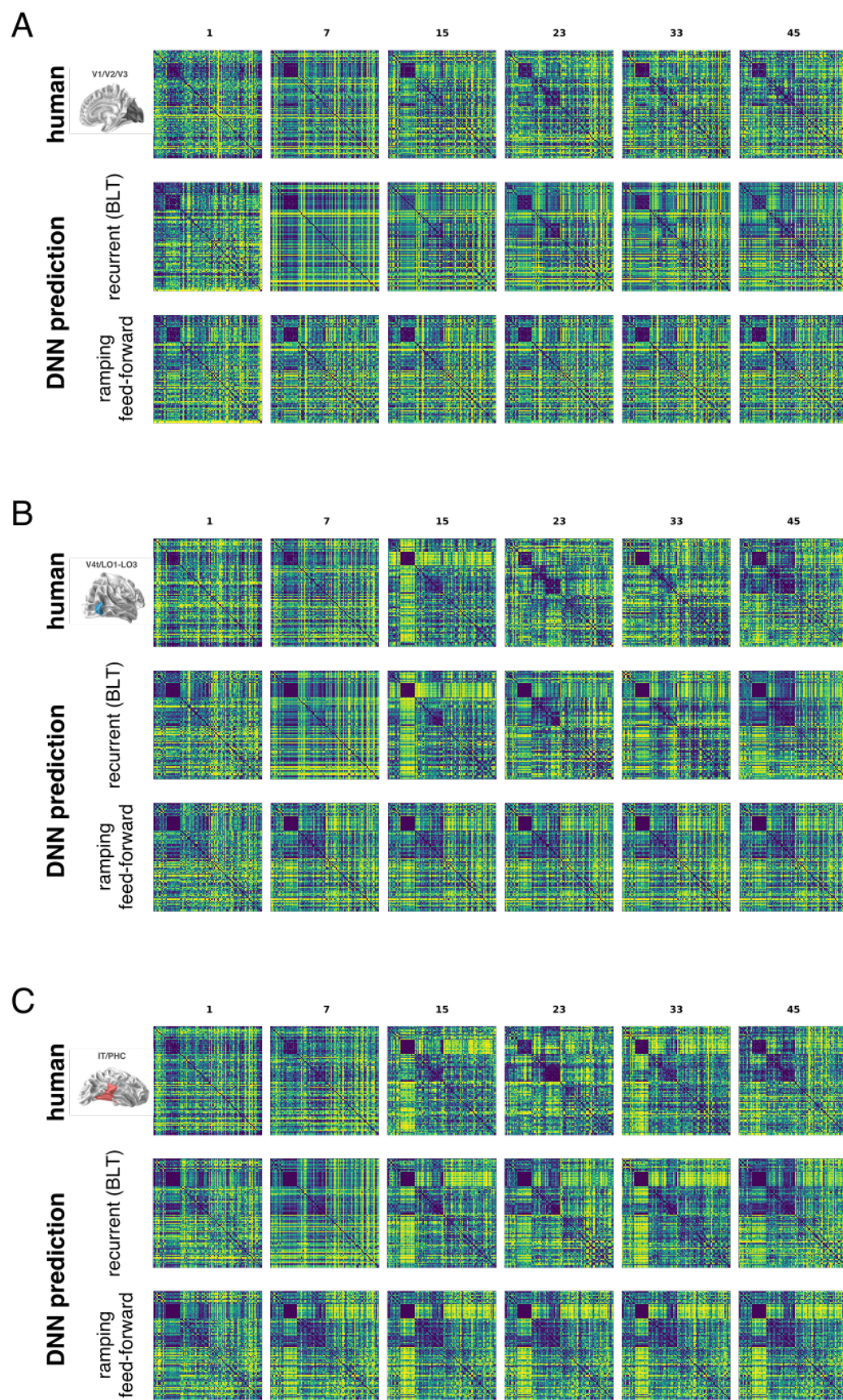
target  
stimulus

RDL training stimulus examples

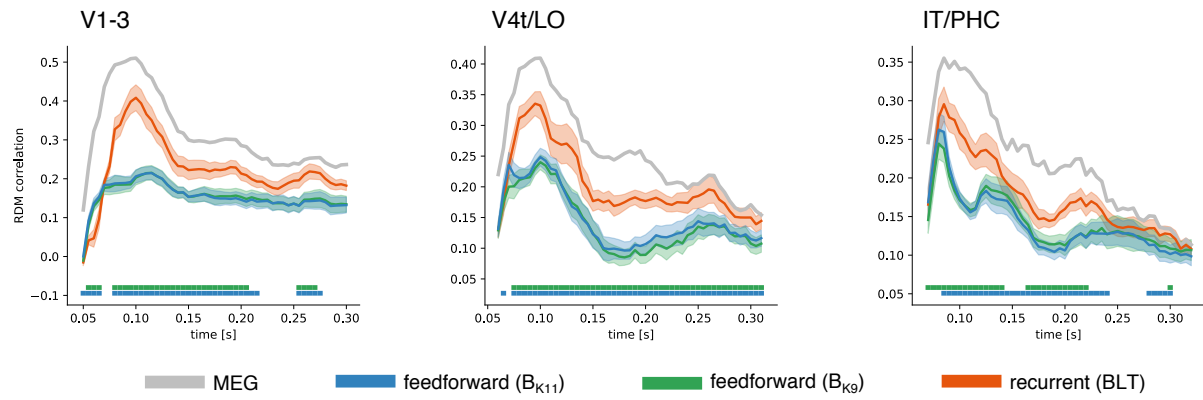


**Supplemental Figure 3.** Example images used for RDL training. The training set consisted of a total of 141k images, matching the categorical structure of the 92 experimental stimuli. 61 categories were included for network training, directly mapping to 89 out of 92 experimental stimuli (3 stimuli were excluded from RDL training due to an insufficient number of training images for training).

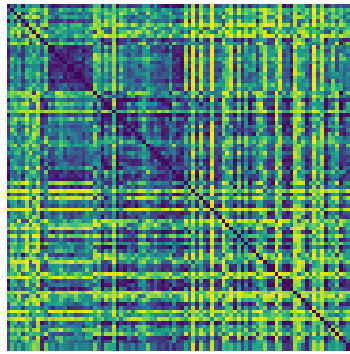




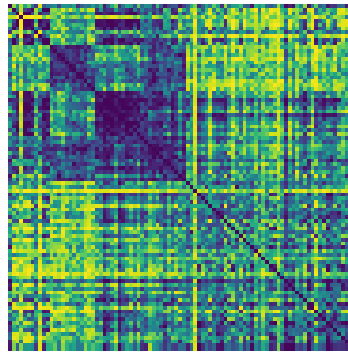
**Supplemental Figure 4.** RDM movie frames for the representational trajectories of the human ventral stream ROIs and model architectures (ramping feedforward and recurrent (BLT) DNNs). A-C show V1-3, V4t/LO, and IT/PHC, respectively.



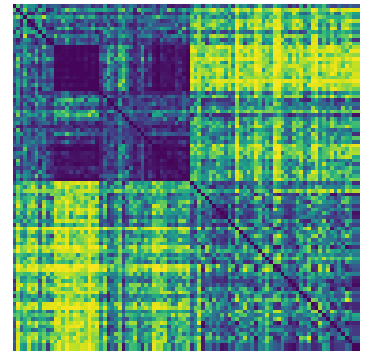
**Supplemental Figure 5.** Frame by frame traces of RDM correlations between DNNs and brain data. Split-half correlation for the MEG data, as used for training, shown in grey.



■ V1-3

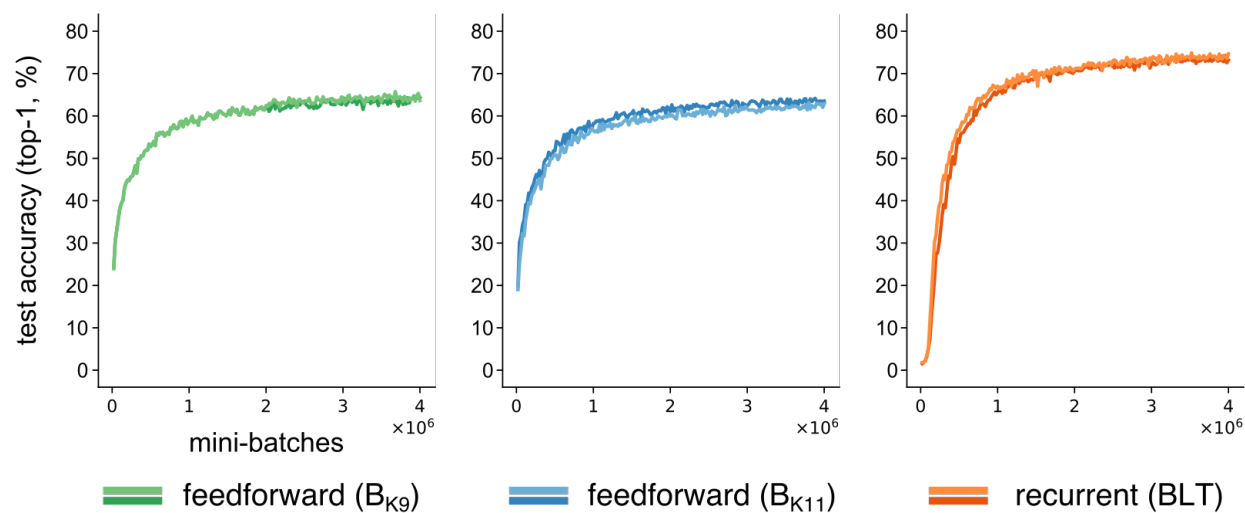


■ V4t/LO



■ IT/PHC

**Supplemental Figure 6.** RDMs extracted from fMRI data obtained from the same participants and the same three ventral stream ROIs.



**Supplemental Figure 7.** Image classification test performance across training for the different model types. Ramping feed-forward (B<sub>K9</sub>, B<sub>K11</sub>; shown in green and blue, respectively) and recurrent (BLT; shown in orange) models.



**Table 1 Network architectural parameters**

Layer	Feature maps	Image size	B <sub>K9</sub> – kernel size (effective)	B <sub>K11</sub> – kernel size (effective)	BLT – kernel size (effective)
1	64	96 × 96	9 (9)	11 (11)	5 (5)
2	64	48 × 48	9 (9)	11 (11)	5 (5)
3	96	24 × 24	9 (9)	11 (11)	5 (5)
4	96	12 × 12	9 (9)	11 (11)	5 (5)
5	128	6 × 6	9 (9)	11 (11)	5 (5)
6	128	3 × 3	9 (5)	11 (5)	5 (5)

**Supplemental Table 1. Details on the network architectures.**

## **Supplementary Movies**

- 1. MEG RDM movies for three ventral stream ROIs.**
- 2. Recurrent DNN RDM movies showing the reconstruction of the representational dynamics observed across three ventral stream ROIs.**
- 3. Feedforward DNN RDM movies showing the reconstruction of the representational dynamics observed across three ventral stream ROIs.**
- 4. MEG, feedforward and recurrent network RDM movies for area V1-3.**
- 5. MEG, feedforward and recurrent network RDM movies for area V4t-LO**
- 6. MEG, feedforward and recurrent network RDM movies for area IT/PHC**